Journal of Power Sources 494 (2021) 229781

Contents lists available at ScienceDirect

Journal of Power Sources

journal homepage: www.elsevier.com/locate/jpowsour

Pseudohalide substitution and potassium doping in $FA_{0.98}K_{0.02}Pb(SCN)_2I$ for high-stability hole-conductor-free perovskite solar cells

Yuren Xia [a,b,1], Cheng Zhao [a,b,1], Peiyang Zhao [a,b,1], Lingyun Mao [a,b], Yucheng Ding [a,b], Daocheng Hong [a], Yuxi Tian [a], Wensheng Yan [c], Zhong Jin [a,b,*]

[a] MOE Key Laboratory of Mesoscopic Chemistry, MOE Key Laboratory of High Performance Polymer Materials and Technology, Jiangsu Key Laboratory of Advanced Organic Materials, School of Chemistry and Chemical Engineering, Nanjing University, Nanjing, 210023, China
[b] Shenzhen Research Institute of Nanjing University, Shenzhen 518063, China
[c] Karlsruhe Institute of Technology, Institute of Microstructure Technology, Karlsruhe, 76344, Germany

ARTICLE INFO

Keywords:
Perovskite solar cells
Pseudohalide substitution
Hole-conductor-free
High-stability

ABSTRACT

Hybrid organic-inorganic halide perovskite solar cells (PSCs) have achieved intriguingly high photoelectric conversion efficiencies (PCEs), but their operational stability is still not satisfactory owing to their vulnerability to moisture and heat. Herein, we report the introduction of pseudohalide thiocyanate ions and potassium dopants into formamidinium lead triiodide ($FAPbI_3$) to obtain a new class of pseudohalide-substituted lead halide perovskites $FAPb(SCN)_2I$ that can be prepared in ambient air and exhibit broad-range light absorption. Through the introduction of K^+-cation doping, hole-conductor-free PSCs based on a $FA_{0.98}K_{0.02}Pb(SCN)_2I$ perovskite light absorber and a low-cost, screen-printable carbon-based counter electrode exhibited a PCE of 13.39%. Importantly, the $FA_{0.98}K_{0.02}Pb(SCN)_2I$-based hole-conductor-free PSCs exhibited an 88% PCE retention even after continuous heating at 100 °C for 1020 h, indicating excellent thermal stability. This study suggests that the compositional engineering of non-iodine X-site pseudohalide anion substitution and A-site cation doping hold great promise for improving the stability of PSCs.

1. Introduction

Perovskite solar cells (PSCs) have attracted enormous interest in the photovoltaic device research field, and the photoelectric conversion efficiency (PCE) of PSCs has increased rapidly to over 25.2% in the past several years [1–7]. PSCs represent a class of promising candidates for next-generation photovoltaic devices owing to their tuneable optical properties, astoundingly high PCE and relatively facile solution-based fabrication process [8–10]. Despite the success in boosting their efficiency, PSCs are still facing several critical challenges, especially their chemical instability in ambient conditions [11,12]. The most studied hybrid lead halide perovskites, such as methylammonium lead triiodide ($MAPbI_3$) and formamidinium lead triiodide ($FAPbI_3$), exhibit very poor stability against moisture and heat. In particular, perovskite materials tend to decompose rapidly in moist air [12–15], which is one of the main barriers for their practical application.

The key to solving the instability issue of PSCs is to find other alternative components to replace the labile iodide anions at the X sites and organic cations (e.g., MA^+ and FA^+) at the A sites of conventional lead halide perovskites. Pseudohalide anions refer to a category of anions formed by two or more nonmetallic atoms and exhibit chemical properties analogous to halogen anions. Thiocyanate is a group of representative pseudohalide compounds composed of S, C and N elements. The SCN^- anions display much better chemical stability than I^- anions in humid air atmospheres and at high temperatures, therefore, it is possible to completely or partially replace the X-site I^- anions by SCN^- anions to significantly improve the moisture stability and heat resistance of PSCs. Herein, we report the design and convenient preparation of a new class of pseudohalide-substituted lead halide perovskite $FAPb(SCN)_2I$ that involves the replacement of two-thirds of the I^- anions in formamidinium lead triiodide ($FAPbI_3$) with SCN^- anions through a convenient two-step sequential solution-phase process. Moreover, we

* Corresponding author. MOE Key Laboratory of Mesoscopic Chemistry, MOE Key Laboratory of High Performance Polymer Materials and Technology, Jiangsu Key Laboratory of Advanced Organic Materials, School of Chemistry and Chemical Engineering, Nanjing University, Nanjing, 210023, China.
E-mail address: zhongjin@nju.edu.cn (Z. Jin).
[1] These three authors contributed equally to this work.

https://doi.org/10.1016/j.jpowsour.2021.229781
Received 8 December 2020; Accepted 8 March 2021
Available online 16 March 2021
0378-7753/© 2021 Elsevier B.V. All rights reserved.

found that the light absorption, optoelectronic properties and thermal stability of $FAPb(SCN)_2I$ can be further improved by potassium-cation doping. With an optimal K^+ doping ratio of 0.02, the $FA_{0.98}K_{0.02}Pb(SCN)_2I$ perovskite film shows the best photovoltaic performance among the $FA_{1-x}K_xPb(SCN)_2I$ samples ($0 \leq x \leq 0.10$). These new mixed-cation perovskites exhibit high absorption coefficients and favourable bandgaps (~1.51 eV) that reach the near-infrared absorption range. Hole-conductor-free PSCs based on a $FA_{1-x}K_xPb(SCN)_2I$ perovskite light absorber and conductive carbon-based counter electrode with a layered configuration comprising fluorine-doped tin oxide (FTO)/compact TiO_2 (*c*-TiO_2)/mesoporous TiO_2 (*m*-TiO_2)/$FA_{1-x}K_xPb(SCN)_2I$/carbon electrode were fabricated in ambient air without the need of strict humidity control. In this device design, a screen-printable, highly stable and cheap carbon counter electrode was used to replace unstable organic hole-transport materials (HTMs) and expensive noble metal electrodes. As a result, the as-optimized $FA_{0.98}K_{0.02}Pb(SCN)_2I$-based hole-conductor-free PSC gained a PCE of 13.39% and remarkable operational stability against heat and humidity, which can be operated normally even after continuous heating at 100 °C for over 1020 h.

2. Results and discussion

The undoped $FAPb(SCN)_2I$ perovskite material containing substituted pseudohalide anions (SCN^-) was prepared by a two-step spin-coating approach using $Pb(SCN)_2$ and FAI precursors, as detailed in the Methods section. By adding a certain amount of KI as a dopant into the precursor mixture, mixed-FA^+/K^+ perovskites with the formula $FA_{1-x}K_xPb(SCN)_2I$ were also synthesized. By adjusting the compositions of the precursor mixture, the optimized ratio of FA^+/K^+ cations was determined to be 0.98:0.02 to achieve the best photovoltaic performance. $MAPb(SCN)_2I$ and $FAPbI_3$ films were also prepared as two control samples via similar methods.

2.1. Structural and compositional analyses

Fig. 1A shows the schematic crystal structure of the undoped perovskite-phase $FAPb(SCN)_2I$ material with a general formula of $FAPbX_3$, in which the X-sites were occupied by SCN^- and I^- ions with a ratio of 2:1. The formation constant of the lead halide complex is essentially its equilibrium constant, which can reflect the binding tightness between the halide ions and the central Pb^{2+} ions [16]. For the PbI_4^{2-} octahedron, the formation constant K_4 (cumulative formation constant $\beta_n = K_1 \times K_2 \times \ldots K_n$) was calculated to be only 3.5 [17], which indicated that the binding of Pb^{2+} and I^- ions was in the range of weak interactions. In the case of $FAPb(SCN)_2I$, the interaction between Pb^{2+} and SCN^- was much stronger, leading to a high formation constant K_4 of

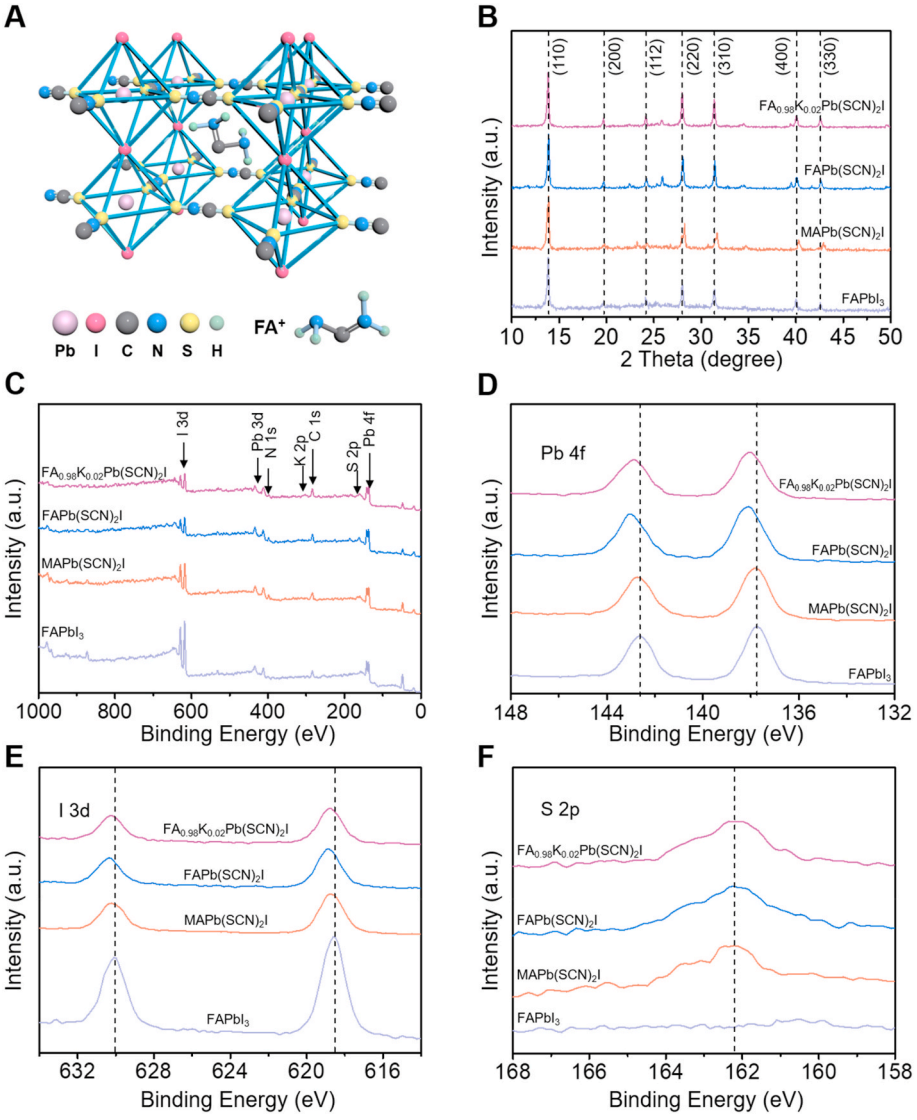

Fig. 1. Structural and compositional characterization of perovskite films. (**A**) Schematic crystal structure of undoped $FAPb(SCN)_2I$ perovskite phase. (**B**) XRD patterns and (**C**) XPS spectra of $FAPbI_3$ (grey lines), $MAPb(SCN)_2I$ (brown lines), $FAPb(SCN)_2I$ (blue lines) and $FA_{0.98}K_{0.02}Pb(SCN)_2I$ (purple lines) films. (**D** to **F**) High-resolution XPS spectra at Pb 4f (D), I 3d (E) and S 2p (F) regions of these samples. (For interpretation of the references to colour in this figure legend, the reader is referred to the Web version of this article.)

up to 7 for the $Pb(SCN)_4^{2-}$ octahedron [18]. Compared to the spherical-shaped Lewis structure of I^- ions, the linear-shaped SCN^- ions with lone pairs of electrons from the S and N atoms can interact strongly with the Pb^{2-} ions and thus can efficiently stabilize the frame structure of $FAPb(SCN)_2I$.

The perovskite films were characterized by X-ray diffraction (XRD) to identify their crystal structures (Fig. 1B). For $FAPbI_3$, the major XRD peaks were located at 13.83°, 19.69°, 28.00° and 31.37°, corresponding to the (110), (200), (220) and (310) planes of the cubic perovskite phase, respectively. Similarly, these peaks were also present in the XRD patterns of $MAPb(SCN)_2I$ (13.88°, 19.80°, 28.24° and 31.68°) and $FAPb(SCN)_2I$ (13.88°, 19.72°, 28.04° and 31.44°), indicating the same cubic-phase crystal structures. The diffraction angles of $FAPb(SCN)_2I$ were slightly larger than those of $FAPbI_3$, suggesting a decrease in the lattice constants due to the substitution of two SCN^- ions. Compared to those for $FAPb(SCN)_2I$, the XRD peaks for $FA_{0.98}K_{0.02}Pb(SCN)_2I$ slightly shifted back to smaller angles (13.84°, 19.68°, 27.96° and 31.36°) owing to the introduction of K^+ doping and the resulting expanded lattice parameters. By comparing the full widths at half maximum (FWHM) of the characteristic (110) diffraction peaks of these samples ($FA_{0.98}K_{0.02}Pb(SCN)_2I$-0.204°, $FAPb(SCN)_2I$-0.208°, $MAPb(SCN)_2I$-0.266°, $FAPbI_3$-0.212°), it could be found that the $FA_{0.98}K_{0.02}Pb(SCN)_2I$ has the smallest FWHM value, indicating its highly ordered crystalline structure. Top-view scanning electron microscopy (SEM) images of the precursor films and perovskite films are shown in Fig. S1. The $Pb(SCN)_2$ and $Pb(SCN)_2$–2%KI precursor films used for the synthesis of $FAPb(SCN)_2I$ and $FA_{0.98}K_{0.02}Pb(SCN)_2I$ exhibited relatively flat surfaces. Notably, the surfaces of all the FA-containing perovskite films contained evenly distributed nanorod arrays, probably due to the preferential growth of perovskite nanocrystals along the vertical orientation.

X-ray photoelectron spectroscopy (XPS) and energy dispersive X-ray spectroscopy (EDX) measurements were performed to study the chemical compositions of these samples, as shown in Fig. 1C–F and Figs. S2–S4. The high resolution XPS spectra of K 2p peaks (Fig. S2C) indicated the successful introduction of K^+ ions. After setting the C 1s peaks of adventitious carbon to 284.6 eV (Fig. S2A), the high-resolution XPS spectra at Pb 4f, I 3d, S 2p, N 1s and K 2p regions were obtained, as shown in Fig. 1D–F and Figs. S2B–S2C, and the characteristic binding energies of these elements were determined and were summarized in Table S1. Compared to those for $FAPbI_3$, the Pb 4f and I 3d peaks for the $MAPb(SCN)_2I$, $FAPb(SCN)_2I$ and $FA_{0.98}K_{0.02}Pb(SCN)_2I$ samples shifted to relatively higher binding energies (Fig. 1D–F), owing to an increase in

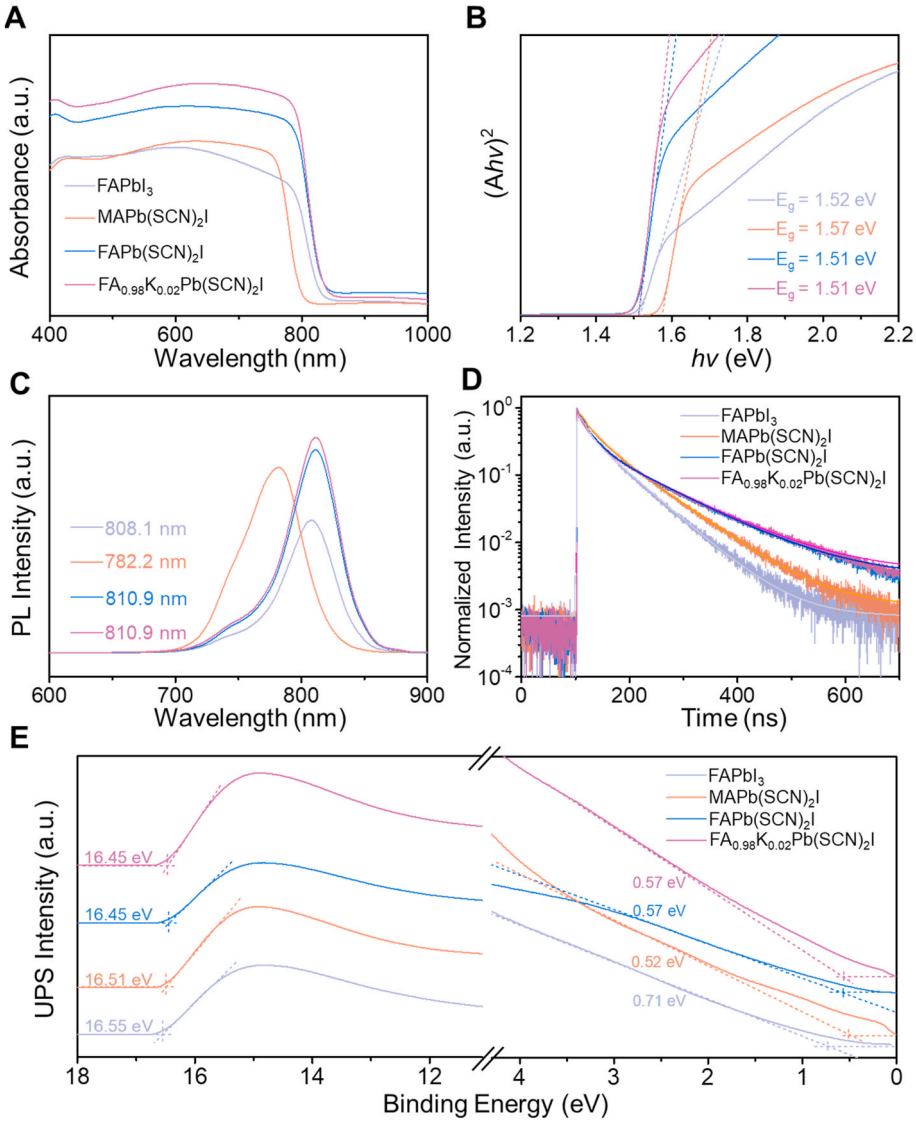

Fig. 2. Photoresponse of as-prepared perovskite films. (**A**) UV–Vis absorption spectra, (**B**) (A$h\nu$) [2] versus $h\nu$ curves, (**C**) PL spectra, (**D**) PL decay curves and (**E**) UPS cutoff spectra of $FAPbI_3$ (grey lines), $MAPb(SCN)_2I$ (brown lines), $FAPb(SCN)_2I$ (blue lines) and $FA_{0.98}K_{0.02}Pb(SCN)_2I$ (purple lines) films. (For interpretation of the references to colour in this figure legend, the reader is referred to the Web version of this article.)

the chemical interaction strength by the introduction of SCN^- ions. Moreover, the intensities of the I 3d peaks of these three samples decreased, and S 2p peaks emerged due to the partial substitution of I^- by SCN^- ions. The uniform distributions of the characteristic elements in the precursor films and perovskite films were confirmed by EDX mapping, as shown in Figs. S3–S4. The atomic concentrations of Pb, S, I and K measured from the EDX results are summarized in Table S2 and the atomic ratio of each element was almost the same as the stoichiometric ratio in the chemical formula of $FA_{0.98}K_{0.02}Pb(SCN)_2I$.

2.2. Photo response

The effects of SCN^- substitution and K^+ doping on the photophysical properties of perovskite films were comprehensively investigated (Fig. 2). The ultraviolet visible-light (UV–Vis) absorption spectrum of $FAPbI_3$ showed a light-absorption edge at a wavelength of ~815 nm, which was larger than that of $MAPb(SCN)_2I$ (~790 nm). Notably, the absorption edges of $FAPb(SCN)_2I$ and $FA_{0.98}K_{0.02}Pb(SCN)_2I$ were measured to be ~820 nm, indicating their narrower bandgaps. Compared to that for $FAPbI_3$, the light absorbance of the $FA_{0.98}K_{0.02}Pb(SCN)_2I$ film with the same thickness was obviously enhanced, which can be ascribed to the introduction of SCN^- and K^+ ions (Fig. 2A). Fig. 2B shows the plots of $(A\hbar\nu)^2$ versus photoenergy ($\hbar\nu$) converted from the UV–Vis absorption spectra. Accordingly, the bandgaps of $FAPbI_3$, $MAPb(SCN)_2I$, $FAPb(SCN)_2I$ and $FA_{0.98}K_{0.02}Pb(SCN)_2I$ were calculated to be 1.52, 1.57, 1.51 and 1.51 eV, respectively. The narrower bandgap of $FAPb(SCN)_2I$ and $FA_{0.98}K_{0.02}Pb(SCN)_2I$ was conducive to light absorption, which was extended from the visible to near-infrared region. Photoluminescence (PL) spectra of $FAPbI_3$, $MAPb(SCN)_2I$, $FAPb(SCN)_2I$ and $FA_{0.98}K_{0.02}Pb(SCN)_2I$ measured at an excitation wavelength of 450 nm are presented in Fig. 2C. Emission peaks at 808.1, 782.2, 810.9 and 810.9 nm were observed and are comparable to the as-measured bandgaps. Fig. 2D presents the PL decay curves of these perovskite films. The intensity-weighted PL decay lifetime τ_{av} of the $FA_{0.98}K_{0.02}Pb(SCN)_2I$ film (84.72 ns) was longer than those of $FAPbI_3$ (53.91 ns), $MAPb(SCN)_2I$ (64.96 ns), and $FAPb(SCN)_2I$ (81.91 ns), confirming the improved charge carrier extraction from $FA_{0.98}K_{0.02}Pb(SCN)_2I$. To investigate the band structures of the samples (Fig. 2E), ultraviolet photoelectron spectroscopy (UPS) analysis was performed by using the He I (21.22 eV) emission line. The energy level of the valence band maximum (E_{VBM}) of a perovskite material is equivalent to its work function (W_s), which can be calculated by the following equation:

$$h\nu - Ws = E_{cutoff} - E_{fermi} \quad (1)$$

where $h\nu$ is the energy of the incident photon (21.22 eV in our case) and E_{cutoff} and E_{fermi} are the binding energies of the secondary electron cutoff and Fermi level, respectively. Therefore, the E_{VBM} values for $FAPbI_3$, $MAPb(SCN)_2I$, $FAPb(SCN)_2I$ and $FA_{0.98}K_{0.02}Pb(SCN)_2I$ were calculated to be −5.38, −5.23, −5.34 and −5.34 eV, respectively. According to the above analyses, the conduction band minimum (E_{CBM}) energy levels for these perovskite materials were determined to be −3.86, −3.66, −3.83 and −3.83 eV, respectively, as illustrated in the energy band diagrams of Fig. S5.

2.3. Device configuration and performance

The as-obtained perovskite films were separately used as light absorbers in the hole-conductor-free PSCs comprising the functional layers of fluorine-doped tin oxide (FTO)/*c*-TiO_2/*m*-TiO_2/perovskite/carbon (Fig. 3A to B). In this device configuration, both expensive noble metal counter electrodes and unstable organic hole transfer materials (HTMs) were replaced by carbon electrodes with high stability, good conductivity, easy processability and low cost [19,20]. The *Ws* of carbon electrodes (−5.0 eV) are similar to gold (−5.1 eV) and thus appropriate for hole collection [21,22]. The energy band levels of hole-conductor-free PSCs with different perovskite light absorbers are presented in Fig. 3C. Owing to the well-matched energy band levels, hole extraction from the VBM of the SCN^--based perovskites to the carbon electrode and electron extraction from the CBM of the SCN^--based perovskites to the *c*-TiO_2/*m*-TiO_2 electron transfer layer (ETL) were expected to proceed smoothly.

The photocurrent density-voltage (*J-V*) curves of the hole-conductor-free PSCs with optimized layer thicknesses of the perovskite light absorbers are shown in Fig. 3D, and the corresponding photovoltaic parameters are summarized in Table S3. The $FAPbI_3$-based hole-conductor-free PSCs exhibited a typical PCE of 8.96%, with a short-circuit density (J_{sc}) of 17.93 mA/cm^2, an open-circuit voltage (V_{oc}) of

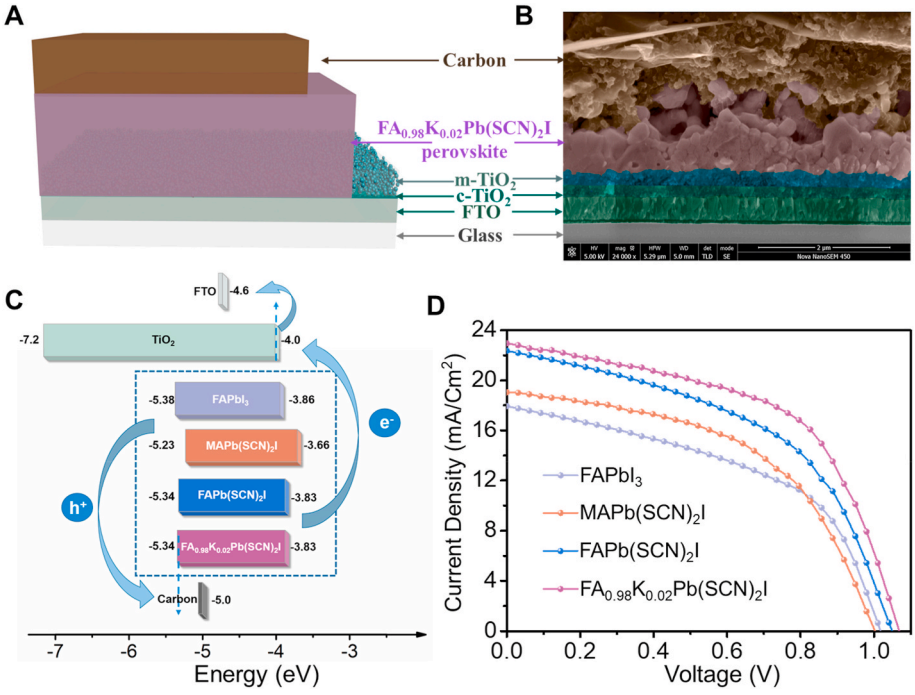

Fig. 3. Device configuration and performance of hole-conductor-free PSCs. (**A**) Schematic structure and (**B**) cross-sectional SEM image of the as-prepared PSCs with the configuration of FTO/*c*-TiO_2/*m*-TiO_2/$FA_{0.98}K_{0.02}Pb(SCN)_2I$/carbon layers. (**C**) Energy level diagrams of the hole-conductor-free PSCs with different perovskite light absorbers. The band levels of different perovskite light absorbers are shown in the blue dashed-line box. (**D**) Typical *J-V* plots of the as-prepared hole-conductor-free PSCs. (For interpretation of the references to colour in this figure legend, the reader is referred to the Web version of this article.)

1.02 V and a fill factor (*FF*) of 0.49. The PCE of the $MAPb(SCN)_2I$-based PSCs (9.70%) was higher than that of $FAPbI_3$ due to the higher J_{sc}, (19.10 mA/cm^2) and *FF* (0.51). However, the V_{oc} of $MAPb(SCN)_2I$ was lower than that of $FAPbI_3$ because of the higher E_{VBM} position of $MAPb(SCN)_2I$. After the introduction of FA^+ ions, the $FAPb(SCN)_2I$-based hole-conductor-free PSCs presented an improved PCE of 11.53%, which was mainly attributed to the clearly increased J_{sc} (22.38 mA/cm^2) and open-circuit voltage (V_{oc}, 1.05 V). Compared to those for the $FAPb(SCN)_2I$-based PSCs, the $FA_{0.98}K_{0.02}Pb(SCN)_2I$-based PSCs displayed increases in all the photovoltaic parameters, including the J_{sc} (22.95 mA/cm^2), V_{oc} (1.07 V), and fill factor (*FF*, 0.55), confirming the beneficial effects of K^+ doping. The PCE of the $FA_{0.98}K_{0.02}Pb(SCN)_2I$-based PSCs reached 13.39%, which is the highest value among these devices. The *J-V* plots of the $FA_{0.98}K_{0.02}Pb(SCN)_2I$-based hole-conductor-free PSCs were measured in the forward and reverse scanning modes (Fig. S6) and indicated a negligible hysteresis. The results of these two scan modes indicated nearly the same performance, with very small differences in the J_{sc} and *FF*. The *J-V* histograms of 56 individual $FA_{0.98}K_{0.02}Pb(SCN)_2I$-based PSCs showed an average PCE value of 11.75%, as summarized in Fig. 4A, Fig. S7 and Table S4. The narrow distribution of the photovoltaic parameters suggested the good repeatability of the device fabrication process.

2.4. Stability

To gain further insights into the chemical stability of pseudohalide-substituted perovskites in ambient environments, hole-conductor-free PSCs were exposed to different humidity levels and temperatures with or without encapsulation. Fig. 4B and Fig. S8 show the photovoltaic parameter retentions of the $FAPb(SCN)_2I$- and $FA_{0.98}K_{0.02}Pb(SCN)_2I$-based PSCs without encapsulation under continuous heating at 100 °C and simultaneous exposure to humid air with a relative humidity (RH) of 70–80%. As shown in Fig. 4B, both curves had a volcano-shaped trend that increased first and then decreased. The peak PCE value for the $FAPb(SCN)_2I$-based PSC appeared at 48 h, and the peak PCE value for the $FA_{0.98}K_{0.02}Pb(SCN)_2I$-based PSC appeared at 24 h. This phenomenon should be due to the increased interfacial contact of the PSCs under higher temperatures, resulting in an apparent increase in J_{sc}. However, the photovoltaic performance of the devices decreased afterwards due to the decomposition of the perovskite caused by moisture infiltration. Apparently, the performance decrease of the PSC based on $FA_{0.98}K_{0.02}Pb(SCN)_2I$ was much slower than that of $FAPb(SCN)_2I$. Throughout the heating process at 100 °C without encapsulation, the V_{oc} of both devices remained very stable, but the J_{sc} had an upward and then downward trend due to the effects of heat and moisture. In addition, the *FF* also declined after heating for a long time. After 120 h under this harsh environment, the normalized PCE of the $FA_{0.98}K_{0.02}Pb(SCN)_2I$-based PSCs still retained 87% of its initial value, which was much better than that of $FAPb(SCN)_2I$ (60%). This indicates that the excellent heat and moisture tolerances of $FA_{0.98}K_{0.02}Pb(SCN)_2I$ originated from the K^+ doping. The time-dependent PCE retentions of the hole-conductor-free PSCs after encapsulation were also measured at room temperature (Fig. 4C and Figs. S9A, C and E) and under continuous heating at 100 °C (Fig. 4D and Figs. S9B, D, and F). In Fig. 4C, the normalized PCE of both the $FAPb(SCN)_2I$- and $FA_{0.98}K_{0.02}Pb(SCN)_2I$-based devices measured at room temperature after encapsulation first trended upward, reaching

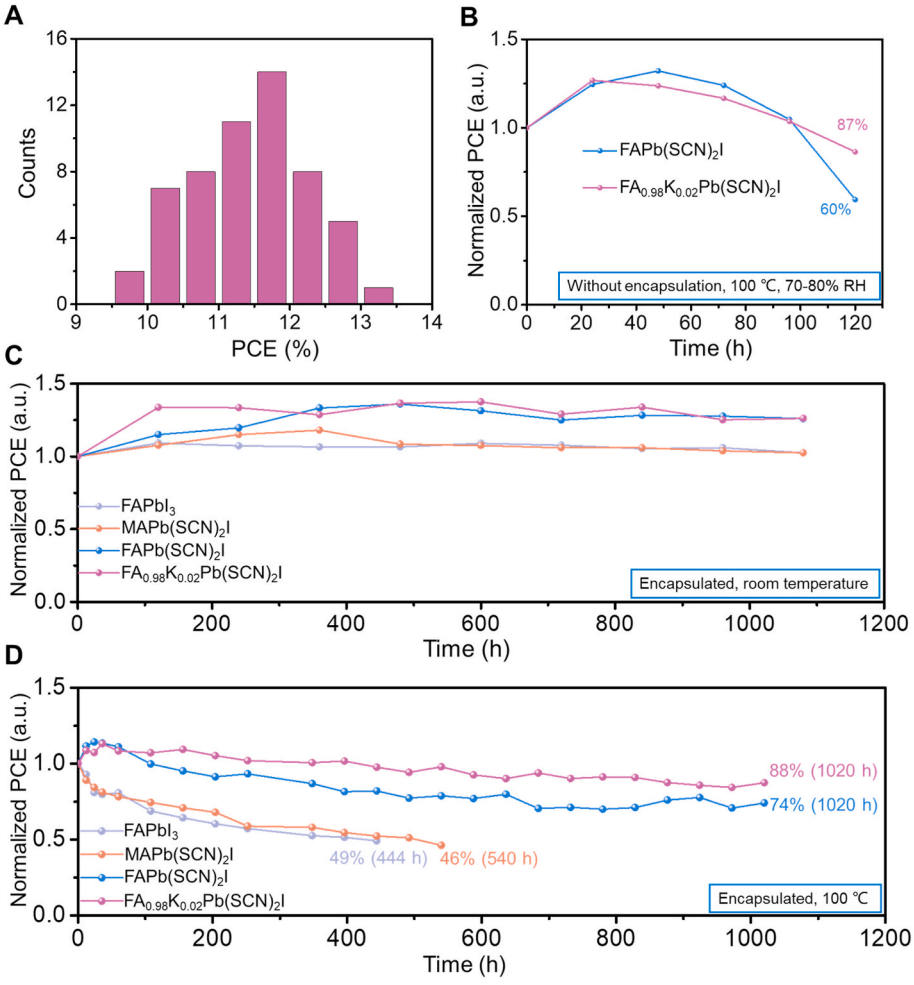

Fig. 4. Stability tests. (**A**) Statistical histogram of PCEs collected from 56 individual $FA_{0.98}K_{0.02}Pb(SCN)_2I$-based hole-conductor-free PSCs. (**B**) Normalized PCE retentions of $FAPb(SCN)_2I$- and $FA_{0.98}K_{0.02}Pb(SCN)_2I$-based PSCs without encapsulation under continuous heating at 100 °C and simultaneous exposure to humid air with a RH of 70%–80%. (**C**) Normalized PCE retention of encapsulated hole-conductor-free PSCs at room temperature. (**D**) Normalized PCE retention of encapsulated hole-conductor-free PSCs under continuous heating at 100 °C.

peak values at 480 h and 600 h, respectively. Then, the PCE values of both devices remained at a relatively stable level. The V_{oc} values of both devices were very stable, the J_{sc} values fluctuated, and the *FF* values first had an upward trend and then tended to be stable. When heated at 100 °C after encapsulation, the PCE retention of the $FAPb(SCN)_2I$- and $FA_{0.98}K_{0.02}Pb(SCN)_2I$-based devices were significantly superior to those of the $FAPbI_3$- and $MAPb(SCN)_2I$-based devices (Fig. 4D). Under constant heating, the V_{oc} of the $FAPb(SCN)_2I$- and $FA_{0.98}K_{0.02}Pb(SCN)_2I$-based devices were almost unchanged, and the J_{sc} degradation of the $FA_{0.98}K_{0.02}Pb(SCN)_2I$-based device was much slower than that of the $FAPb(SCN)_2I$-based device, while the *FF* of the $FAPb(SCN)_2I$-based device remained at a higher level than that of the $FA_{0.98}K_{0.02}Pb(SCN)_2I$-based device. Overall, the $FA_{0.98}K_{0.02}Pb(SCN)_2I$-based device showed the highest PCE retention among all the devices. After being continuously heated at 100 °C for 1020 h, the encapsulated $FA_{0.98}K_{0.02}Pb(SCN)_2I$-based PSC still maintained ~88% of its initial performance (Fig. 4D), which was far better than those of the $FAPb(SCN)_2I$-based PSCs (~74% after 1020 h), $MAPb(SCN)_2I$-based PSCs (~46% after 540 h) and $FAPbI_3$-based PSCs (~49% after 444 h). $FAPbI_3$ would gradually degenerate to precursors when being continuously heated at 100 °C, and this would greatly affect its absorption of sunlight, resulting in a rapid decrease in PCE [23]. Similarly, $MAPbI_3$ has the same problem and its degeneration rate is much rapider than that of $FAPbI_3$. Interestingly, we noticed that the substitution of SCN^- can greatly increase the stability of perovskite film, and the PCE of $MAPb(SCN)_2I$-based PSCs could maintain 46% after being heated for 540 h. Moreover, according to the XRD patterns in Fig. 1B, $FA_{0.98}K_{0.02}Pb(SCN)_2I$ has higher crystalline degree and fewer defects than $FAPb(SCN)_2I$, which could further reduce the degeneration rate of perovskites. In result, the $FA_{0.98}K_{0.02}Pb(SCN)_2I$ based PSCs exhibit higher PCE retention even after being heated for 1020 h. These test results confirmed the favourable thermal stability of $FA_{0.98}K_{0.02}Pb(SCN)_2I$, suggesting that the introduction of K^+ ions was conducive to maintaining a good perovskite structure and crystallinity at high temperatures.

2.5. Effects of K^+ doping ratios

To evaluate the effect of K^+-doping concentration, $FA_{1-x}K_xPb(SCN)_2I$ perovskite films with different x ratios were prepared. With an increase in the K^+-doping ratio, the morphologies of the perovskite films appeared to become staggered, as revealed by the SEM images in Fig. S10. The light absorbance and crystalline structure of the $FA_{1-x}K_xPb(SCN)_2I$ perovskite films were compared according to their UV–vis absorption spectra, $(Ahv)^2$-hv curves and XRD patterns (Fig. 5A–C). The $FA_{0.98}K_{0.02}Pb(SCN)_2I$ perovskite film showed the strongest absorption intensity (Fig. 5A) and the absorption edges of the $FA_{1-x}K_xPb(SCN)_2I$ perovskite films were measured to be ~820 nm, corresponding to a bandgap of ~1.51 eV (Fig. 5B). By comparing the XRD patterns of $FAPb(SCN)_2I$ (x = 0) and $FA_{0.98}K_{0.02}Pb(SCN)_2I$ (x = 0.02) (Fig. 5C), the full width at half maximum (FWHM) of the characteristic (110) peak was decreased from 0.208° to 0.204° after the introduction of K^+ doping, indicating an increase of crystalline degree. However, when the K^+ doping ratio further increased to 0.04, the FWHM increased from 0.204° to 0.206°, suggesting that the crystalline degree was decreased. Moreover, two weak impurity peaks at approximately 12.6° and 11.7° (belonged to PbI_2 and δ-$FAPbI_3$, respectively) appeared in the XRD patterns of 0.06–0.10 doping ratios, indicating that the relatively high K^+ doping ratios might result in the phase separation of the perovskite film. As shown in Fig. 5D, the hole-conductor-free perovskite solar cell based on $FA_{0.98}K_{0.02}Pb(SCN)_2I$ had the maximum V_{oc}, J_{sc} and *FF* values, thus presenting the highest photovoltaic performance among the $FA_{1-x}K_xPb(SCN)_2I$ samples. However, as the K^+-doping concentration increased from 0.04 to 0.10, the V_{oc} remained almost unchanged, but J_{sc} and *FF* obviously decreased, leading to a decrease in the PCE value from 10.77% to 7.98%, respectively, as summarized in Table S5. This indicated that the phase separation resulting from an excessively high K^+-doping concentration had a negative effect on the photovoltaic performance.

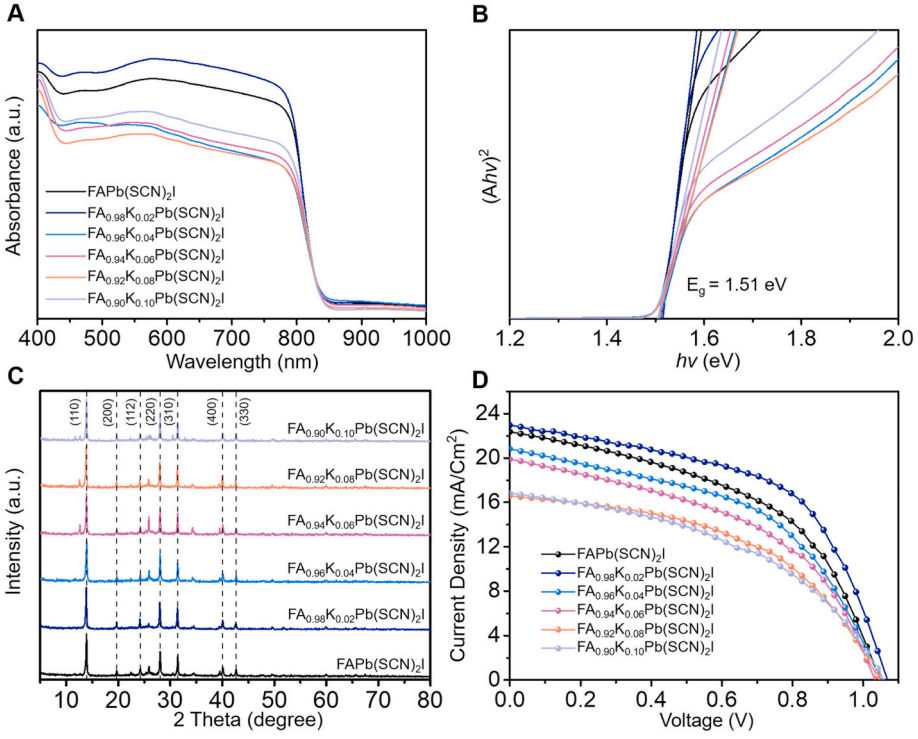

Fig. 5. The effects of different K^+ doping ratios. (**A**) UV–vis spectra, (**B**) (A*hv*) [2] versus *hv* curves, (**C**) XRD patterns and (**D**) *J-V* plots of the $FA_{1-x}K_xPb(SCN)_2I$-based hole-conductor-free PSCs, in which the K^+ ion doping ratios were x = 0, 0.02, 0.04, 0.06, 0.08 and 0.10.

3. Conclusion

In summary, we propose the design and preparation of a new type of pseudohalide-substituted perovskite material $FAPb(SCN)_2I$ via a two-step sequential solution-phase process. The replacement of two X-site I^- anions in a conventional $FAPbI_3$ by two thiocyanate anions drastically improved the tolerance against heat and moisture. The $FAPb(SCN)_2I$ perovskite had a suitable band gap (~1.51 eV) and superb energy band positions, which enabled the light absorption to reach the near-infrared region. Through further K^+-cation doping, mixed-FA^+/K^+ cation perovskite $FA_{1-x}K_xPb(SCN)_2I$ films were prepared by partially replacing the FA^+ ions in $FAPb(SCN)_2I$ with K^+ ions. The hole-conductor-free PSCs based on the $FA_{0.98}K_{0.02}Pb(SCN)_2I$ light absorber and screen-printable carbon counter electrode exhibited a good photovoltaic performance and an outstanding long-term stability and resistibility against heat and moisture. These PSCs are much easier and less expensive to manufacture due to the use of conductive carbon electrodes instead of expensive organic HTMs and noble metal counter electrodes; they also possess a high reproducibility and convenient fabrication. This work helps to tackle the intractable issue regarding the intrinsic thermal and moisture instability of lead halide perovskite materials through rational composition design, which represents a feasible strategy towards realizing highly stable hybrid perovskite materials and devices for further optoelectronic conversion applications.

4. Experimental section

4.1. Materials and chemicals

Formamidinium iodide (FAI, >99%), methylammonium iodide (MAI, >99%) and 4-*tert*-butylpyridine (≥96.0%) were purchased from Liaoning Youxuan Energy & Technology Co. Ltd, China. Lead thiocyanate ($Pb(SCN)_2$, 99.5%) was purchased from Sigma-Aldrich. Bis(trifluoromethane)sulfonimide lithium salt (Li-TFSI, >98%), *N, N*-dimethylformamide (DMF, 99.8%) and lead iodide (PbI_2, 99.9985%) were purchased from Alfa Aesar. Titanium isopropoxide (95%), isopropanol (99.5%), potassium iodide (KI, 99%) and zinc powder (Zn, 99.99%) were purchased from Aladdin. All chemicals were used without further purification.

4.2. Preparation of c-TiO_2 and m-TiO_2 layers on FTO substrates

The FTO glass substrates were first etched by Zn powder and 4.0 M HCl to produce desirable patterns. Then, the patterned FTO substrates were sequentially cleaned by ultrasonication in acetone, ethanol and pure water for 15 min. Subsequently, a thin c-TiO_2 layer was deposited on the FTO substrates by spin-coating an ethanol solution of titanium isopropoxide (0.5 M) and diethanol amine (0.5 M) at 7000 rpm for 30 s, followed by annealing in air at 500 °C for 2 h. The m-TiO_2 layer was deposited on the c-TiO_2 layer by spin-coating a mixture of TiO_2 nanoparticle paste (with an average diameter of 20 nm) and ethanol with a weight ratio of 1:8 at 5000 rpm for 30 s, dried at 120 °C for 10 min, and then annealed at 500 °C for 30 min. Then, the substrates were soaked in an aqueous solution of 40 mM $TiCl_4$ at 70 °C for 30 min, cleaned with water and ethanol, and then annealed at 450 °C for another 30 min.

4.3. Preparation of hole-conductor-free PSCs based on $FA_{0.98}K_{0.02}Pb(SCN)_2I$ films

All the fabrication steps for the $FA_{0.98}K_{0.02}Pb(SCN)_2I$-based PSCs were conducted in ambient air (with a RH of 40–50%). Typically, a precursor mixture of 2.0 mmol $Pb(SCN)_2$ and 0.04 mmol KI was dissolved in 1.0 mL of *N, N*-dimethylformamide (DMF) and stirred at 80 °C for 1 h. Then, the solution was deposited on the FTO/c-TiO_2/m-TiO_2 substrate by spin-coating at 3000 rpm for 30 s. The substrate was immediately dipped into an isopropanol solution of 15 mg/mL formamidine iodide (FAI) for 10 min. Subsequently, the as-obtained black films were heated on a hotplate at 210 °C in ambient air for 1 min. Then, the counter electrode was deposited on the perovskite layer by a doctor-blade or silk-screen printing of a conductive carbon paste and then heated at 70 °C for 60 min. For encapsulation, the PSCs were sealed by a cover glass and hot-melt spacer (30 μm thick, Surlyn 1702, Solaronix).

4.4. Preparation of PSCs based on the $FAPb(SCN)_2I$, $MAPb(SCN)_2I$ and $FAPbI_3$ films as control samples

In contrast, the deposition procedure of the $FAPb(SCN)_2I$ film was similar to that of the $FA_{0.98}K_{0.02}Pb(SCN)_2I$ film, except that the mixture of $Pb(SCN)_2$ and KI was replaced by 2.0 mmol of $Pb(SCN)_2$. The deposition procedure of the $MAPb(SCN)_2I$ film was similar to that of the $FAPb(SCN)_2I$ film, except that the FAI precursor was replaced by MAI and the substrate was heated at 105 °C (instead of 210 °C) for 5 min to obtain a black $MAPb(SCN)_2I$ film. The deposition procedure of the $FAPbI_3$ film was also similar to that of the $FAPb(SCN)_2I$ film, except that the $Pb(SCN)_2$ precursor was replaced by 1.0 mmol of PbI_2, and the substrate was heated at 150 °C (instead of 210 °C) for 20 min to obtain a black $FAPbI_3$ film.

4.5. Material characterizations

The XRD spectra were obtained by a Bruker D-8 Advance diffractometer with a Cu *Kα* X-ray source. Both the top-view and cross-sectional SEM images were obtained with FEI Nano Nova-450. The EDX analysis was performed with a Bruker QUANTAX accessory attached to the scanning electron microscope (SEM). XPS analyses were carried out with a PHI-5000 VersaProbe X-ray photoelectron spectrometer with an Al *Kα* X-ray source. UPS spectra were obtained with a Thermo Fisher Scientific K-ALPHA$^+$ instrument by using the He I (21.22 eV) emission line. Before the photovoltaic tests, the PSCs were illuminated under simulated AM 1.5G solar light using a solar simulator (100 mW/cm^2, NOWDATA SXDN-150E) for 15 min in advance for activation. The UV–vis absorbance spectra of the perovskite films were measured by a Shinadzu UV-2456 spectrophotometer. The PL spectra and PL decay curves were recorded on a home-built wide-field fluorescence microscope under an excitation wavelength of 450 nm. The *J-V* curves were measured with a Keithley 2400 Source Meter under simulated AM 1.5G illumination. The light intensity was calibrated with a standard single-crystalline Si solar cell. Typically, the active area of the PSCs in this study was 0.09 cm^2. Both forward and reverse scans were measured with a scanning speed of 200 mV/s.

Author contributions

Z. J. conceived the idea and designed the experiments. Y.R. X, P.Y. Z. and C. Z. performed the material synthesis and fabricated the devices. Y. R. X., P.Y. Z., C. Z., L.Y. M. and Y.C. D. contributed to the XPS, UPS, SEM, UV–Vis absorption and XRD characterizations. Y.R. X. and C. Z. tested the photovoltaic performances of PSCs. D.C. H. and Y.X. T. carried out the PL characterizations. Y.X. T. and W.S. Y. helped data analysis. Y.R. X., P.Y. Z., C. Z. and Z. J. analyzed the data and wrote the paper. Z. J. supervised this project. All authors discussed the results and commented on the manuscript.

Data and materials availability

The data that support the findings of this study are available from the corresponding author upon reasonable request.

Declaration of competing interest

The authors declare that they have no known competing financial

interests or personal relationships that could have appeared to influence the work reported in this paper.

Acknowledgments

This work was supported by the National Key Research and Development Program of China (2017YFA0208200), the Fundamental Research Funds for the Central Universities of China (0205-14380219, 0205-14913212), the Projects of Natural Science Foundation of China (22022505, 21872069, 51761135104), the Natural Science Foundation of Jiangsu Province (BK20180008), and the Shenzhen Fundamental Research Program of Science, Technology and Innovation Commission of Shenzhen Municipality (JCYJ20180307155007589).

Appendix A. Supplementary data

Supplementary data to this article can be found online at https://doi.org/10.1016/j.jpowsour.2021.229781.

References

[1] A. Kojima, et al., Organometal halide perovskites as visible-light sensitizers for photovoltaic cells, J. Am. Chem. Soc. 131 (2009) 6050–6051.
[2] H.-S. Kim, et al., Lead iodide perovskite sensitized all-solid-state submicron thin film mesoscopic solar cell with efficiency exceeding 9%, Sci. Rep. 2 (2012) 591.
[3] M.M. Lee, et al., Efficient hybrid solar cells based on meso-superstructured organometal halide perovskites, Science 338 (2012) 643–647.
[4] J. Burschka, et al., Sequential deposition as a route to high-performance sensitized solar cells, Nature 499 (2013) 316.
[5] W. Chen, et al., Efficient and stable large-area perovskite solar cells with inorganic charge extraction layers, Science 350 (2015) 944.
[6] N. Jeon, et al., A fluorene-terminated hole-transporting material for highly efficient and stable perovskite solar cells, Nat. Energy 3 (2018) 682–689.
[7] accessed, https://www.nrel.gov/pv/cell-efficiency.html. (Accessed July 2020).
[8] P. Gao, et al., Organohalide lead perovskites for photovolataic applications, Energy Environ. Sci. 7 (2014) 2448–2463.
[9] J. Snaith, H. Perovskite, The emergence of a new era for low-cost, high-efficiency solar cells, J. Phys. Chem. Lett. 4 (2013) 3623–3630.
[10] N.G. Park, Organometal perovskite light absorber toward a 20% efficiency low-cost solid-state mesoscopic solar cell, J. Phys. Chem. Lett. 4 (2013) 2243–2429.
[11] T. Leijtens, et al., Overcoming ultraviolet light instability of sensitized TiO_2 with meso-superstructured organometal tri-halide perovskite solar cells, Nat. Commun. 4 (2013) 2885.
[12] G.D. Niu, et al., Study on the stability of $CH_3NH_3PbI_3$ films and the effect of post-modification by aluminum oxide in all-solid-state hybrid solar cells, J. Mater. Chem. A. 2 (2014) 705–710.
[13] A. Abate, et al., Supramolecular halogen bond passivation of organ-inorganic halide perovskite solar cells, Nano Lett. 14 (2014) 3247–3254.
[14] J.L. Yang, et al., Investigation of $CH_3NH_3PbI_3$ degradation rates and mechanisms in controlled humidity environments using in situ techniques, ACS Nano 9 (2015) 1955–1963.
[15] F. Bella, et al., First pseudohalogen polymer electrolyte for dye-sensitized solar cells promising for in situ photopolymerization, J. Phys. Chem. C 117 (2013) 20421–20430.
[16] Q.L. Jiang, et al., Pseudohalide-induced moisture tolerance in perovskite $CH_3NH_3Pb(SCN)_2I$ thin films, Angew. Chem. 127 (2015) 7727–7730.
[17] H.L. Clever, et al., The solubility of some sparingly soluble lead salts: an evaluation of the solubility in water and aqueous electrolyte solution, J. Phys. Chem. Ref. Data 9 (1980) 751–784.
[18] G.W. Leonard, et al., Thiocyanate complexes of lead and thallium in solution, J. Phys. Chem. 60 (1956) 1493–1495.
[19] J. Liang, et al., All-inorganic perovskite solar cells, J. Am. Chem. Soc. 138 (2016) 15829.
[20] J. Liang, et al., $CsPb_{0.9}Sn_{0.1}IBr_2$ based all-inorganic perovskite solar cells with exceptional efficiency and stability, J. Am. Chem. Soc. 139 (2017) 14009.
[21] A. Mei, et al., A hole-conductor-free, fully printable mesoscopic perovskite solar cell with high stability, Science 345 (2014) 295.
[22] L. Etgar, et al., Mesoscopic $CH_3NH_3PbI_3/TiO_2$ heterojunction solar cells, J. Am. Chem. Soc. 134 (2012) 17396.
[23] S. Emanuele, et al., Stability of solution-processed $MAPbI_3$ and $FAPbI_3$ layers, Phys. Chem. Chem. Phys. 18 (2016) 13413.